Experimental characterization of a section of a spherically imploding plasma liner formed by merging hypersonic plasma jets

K. C. Yates,[1, 2, a)] S. J. Langendorf,[1, b)] S. C. Hsu,[1, c)] J. P. Dunn,[1] S. Brockington,[3, 4] A. Case,[3, 4] E. Cruz,[3, 4] F. D. Witherspoon,[3, 4] Y. C. F. Thio,[4] J. T. Cassibry,[5] K. Schillo,[5] and M. Gilmore[2]

[1)] *Physics Division, Los Alamos National Laboratory, Los Alamos, NM 87545, USA*

[2)] *Electrical and Computer Engineering Department, University of New Mexico, Albuquerque, NM 87131, USA*

[3)] *HyperV Technologies Corp., Chantilly, VA 20151, USA*

[4)] *HyperJet Fusion Corporation, Chantilly, VA 20151, USA*

[5)] *Propulsion Research Center, University of Alabama in Huntsville, Huntsville, AL 35899, USA*

(Dated: 6 November 2021)

We report experimental results on merging of hypersonic plasma jets, which is the fundamental building block for forming spherically imploding plasma liners as a potential standoff compression driver for magneto-inertial fusion. Jets are formed and launched by contoured-gap coaxial plasma guns mounted at the six vertices and the center of a hexagon covering approximately one-tenth of the surface area of a 9-ft.-diameter spherical chamber. First, from experiments with two and three merging jets of four different species (N, Ar, Kr, Xe), we show that (1) density spatial non-uniformities can be large (with electron-density jumps ranging from 2.9 for N to 6.6 for Xe) when shocks form upon jet merging, but smaller (density jumps <2) when shocks do not form; (2) jet impurities (20% Ti in these experiments) can increase the level of density spatial non-uniformity by increasing the collisionality of jet merging, leading to shock formation rather than potentially more desirable shockless jet merging; and (3) the liner Mach number can remain high ($\gtrsim 10$), as required for plasma liners to be an effective compression driver. Second, from experiments with six and seven merging jets using Ar, we present results with improved jet-to-jet mass balance of <2% across jets, including (1) evidence of substantially increased balance in the jet merging and symmetry of the liner structure, and (2) potentially favorable changes in the jet-merging morphology with the addition of the seventh jet. For both experiments, we present comparisons between experimental and synthetic data from three-dimensional hydrodynamic codes.

I. INTRODUCTION

Magneto-inertial fusion (MIF), aka magnetized target fusion (MTF), is a class of pulsed fusion approaches in which an imploding liner compresses a magnetized target plasma to fusion conditions,[1–4] at ion densities intermediate between those of magnetic and inertial fusion. Many MIF embodiments have been pursued over a period spanning more than forty years, e.g., the development of rotating cylindrical liquid liners[5,6] intended to compress a field-reversed configuration, MAGnitnoye Obzhatiye (MAGO) or magnetic compression,[7] cylindrical solid-liner compression of an FRC,[8,9] acoustically driven liquid-liner compression of a spherical tokamak,[10] and magnetized liner inertial fusion[11,12] (MagLIF, which is a cylindrical solid-liner compression of a laser-preheated magnetized plasma). MagLIF provided a definitive demonstration of proof-of-concept for MIF by achieving multi-keV temperatures[12] and BR (product of magnetic field times fuel radius) values[13] approaching those needed for fuel self-heating from energy deposition by fusion-produced α particles.[14] To meet the economic requirements of a power plant, it may be necessary for an MIF embodiment to have high repetition rate (e.g., ~ 1 Hz) and low cost per shot (e.g., few cents/shot amortized over the life of the power plant). This tends to favor liquid and plasma liners, which avoid the repetitive mass destruction associated with solid liners that lead to lower repetition rate and higher cost per shot.

Since 2009, a multi-institutional collaboration led by Los Alamos National Laboratory (LANL) has been exploring the development of a high-shot-rate, low cost-per-shot compression driver for MIF based on the concept of plasma-jet-driven MIF, or PJMIF,[15–22] in which a spherically imploding plasma liner is formed via merging hypersonic plasma jets. The chief advantages of PJMIF are (1) high implosion speeds (> 50 km/s) to overcome the rate of energy loss in the magnetized plasma target and (2) several-meter standoff of the plasma-formation hardware (plasma guns) to allow for reasonably long periods between maintenance or replacement in a power plant. The key disadvantages of PJMIF are the early stage of development and challenges in forming both the spherically imploding plasma liner[19,23] and a compatible magnetized plasma target.[24] Furthermore, merging plasma jets will seed non-uniformities in the liner that could lead to intolerable levels of Rayleigh-Taylor insta-

[a)] kyates@lanl.gov

[b)] samuel.langendorf@lanl.gov

[c)] scotthsu@lanl.gov

bility and liner/fuel mix when the heavier liner decelerates against the lighter target plasma. The amount of liner non-uniformity resulting from merging plasma jets and the amount that can be tolerated for PJMIF to remain viable are both open research questions. Plasma liners may also have limited hydrodynamic efficiency in transferring energy to the target due in part to radial expansion of the liner during implosion.[21]

A body of published literature lays out the theoretical issues and numerical scaling-studies of plasma-liner formation and implosion via merging hypersonic plasma jets.[15,18–21,23,25–31] Previous research on the LANL Plasma Liner Experiment (PLX),[19,32] using parallel-plate mini-railguns developed by HyperV Technologies Corp.,[33–36] studied single plasma-jet propagation,[37] two-jet oblique merging,[38,39] and two-jet head-on merging.[40] These earlier experiments led to the identification and characterization of plasma shock formation between merging jets that was shown to be consistent with hydrodynamic oblique shock theory.[38,39] The merging of head-on plasma jets was shown to lead to slightly higher electron temperature T_e and mean-charge-state $\bar{Z}$, tending to reduce the counter-streaming ion–ion mean free path and increasing the collisionality of the jet merging.[40]

The aim of this work is to characterize in detail the merging of up to seven hypersonic plasma jets launched by new contoured-gap coaxial guns[22,41] developed under the ARPA-E ALPHA program.[42] First, we report results from two- and three-jet merging experiments repeated for different gas species (N, Ar, Kr, Xe), augmenting recent shock-ion-heating studies,[43,44] which are based on some of the same experimental campaigns presented here. As mentioned earlier, plasma-jet merging generates non-uniformities upon formation of the imploding plasma liner, leading to strong, localized ion heating[43] and an impulsive increase in the ion sound speed C_s and decrease in Mach number M. This degrades the liner's ability to effectively compress a magnetized fusion target. This work provides experimental data on the plasma parameters and new understanding of shock-formation dynamics and evolution of M during two- and three-jet merging. Second, we evaluate the symmetry in a section of the spherically imploding plasma liner that is formed by merging six and seven hypersonic plasma jets with reduced ($< 2\%$) jet-to-jet mass variation across all the jets, as compared to earlier results with $> 20\%$ mass variation across six jets.[41] While merging two and three plasma jets is the most fundamental building block for forming spherically imploding plasma liners via merging plasma jets, the merging of six and seven jets covering approximately one-tenth of the surface area of a sphere is the next step toward evaluating the macro-structure and morphology of a section of the plasma liner. The data presented include time- and space-resolved electron density n_e and T_e measurements from interferometry and survey spectroscopy, respectively, and end-on images of six- and seven-jet merging. All of the data presented in this paper are being used to benchmark multi-physics models and codes[45,46] to further evaluate plasma-jet merging, plasma-liner formation, and the PJMIF concept.[15,19,22]

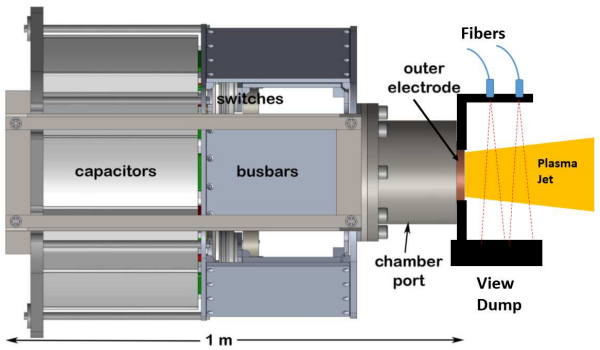

FIG. 1. The coaxial plasma gun used in these experiments, with an integrated -5-kV (negative polarity on the inner electrode), 575-μF capacitor bank driving the gun electrodes. The timing and speed of each plasma jet are measured by fiber-coupled photodiodes with viewing sightlines separated by 2 cm as shown.

The paper is organized as follows. Section II describes the experimental and diagnostic setups for both the two/three and six/seven jet-merging experiments. Sections III and IV present results and discussion of the two/three and six/seven jet-merging experiments, respectively. Section V provides a summary and conclusions. Appendix A includes the N, Kr, and Xe data associated with Sec. III, and Appendix B presents details on the improved jet-to-jet balance associated with Sec. IV.

II. EXPERIMENTAL SETUP

A. PLX facility and diagnostics

Many details about PLX, on which the present experiments were performed, have been presented elsewhere.[22,32,37,41,44] Here, we summarize the particular details pertinent to this paper. PLX has a 9-ft.-diameter, stainless-steel spherical vacuum chamber. For this work, seven coaxial plasma guns are mounted on the chamber in a hexagonal pattern (with six guns on the vertices and one in the middle), covering roughly one-tenth of the surface area of the spherical vacuum chamber.

The coaxial plasma guns (Fig. 1) are designed and built by HyperV Technologies Corp. and described in detail elsewhere.[41] In these experiments, initial plasma-jet densities are $n_i \sim 10^{16}$ cm^{-3}, $T_e \approx 1.5$ eV, $\bar{Z} \approx 1$–2, speed $v_{\rm jet} \approx 50$ km/s, and $M = v_{\rm jet}/C_s \gtrsim 10$. The banks driving each set of gun electrodes and all the gas valves (GV), pre-ionization (PI), and electrode-bank master-trigger (MT) systems used peak voltages of -4.5, 8.5, 24, and -28 kV, respectively, with capacitances of 575, 96, 6, and 6 μF, respectively (note that there is a separate electrode bank for each gun, but all seven guns share the GV,

PI, and MT banks). The GV capacitor bank is triggered at $t = -600$ to -300 μs, PI bank triggered at $t = -20$ μs, and gun-electrode banks at $t = 0$.

The diagnostic suite includes a twelve-chord interferometer, visible survey spectrometer, high-resolution Doppler spectrometer, photodiode array at each gun nozzle to measure jet speed, and a single-frame camera with an intensified charge-coupled-device (iCCD) detector The interferometer uses a 320-mW, 651-nm solid-state laser in a heterodyne configuration, which is an upgrade from the previous eight-chord system.[47,48] Each probe beam is approximately 0.3 cm in diameter, which sets the spatial resolution transverse to each chord. Visible survey spectroscopy is fielded with 0.160-nm/pixel resolution at 510 nm and coupled to a PI-MAX2 intensified charged-couple-device (iCCD) camera, with a typical exposure of 1–2 μs and a field-of-view of 1–2 cm in diameter. High-resolution spectroscopy is fielded using a 4-m McPherson 2062DP, with 2400-mm^{-1} grating and 1.52 pm/pixel at 480.6 nm. The 4-m spectrometer is coupled to a Stanford Computer Optics 4 Quik E iCCD with typical exposure time of 1 μs and a field-of-view of 1–2 cm in diameter. The survey and high-resolution spectrometer viewing optics (one chord each) are moved when necessary to different positions between shots. Two light-collecting optical fibers separated by 2 cm were installed near the exit of each gun as shown in Fig. 1. Light is collected through a 1-mm, 5/16-in.-deep pinhole with SH-4001 fibers and relayed to a 100-MHz digitizer board, which provides jet velocity via time-of-flight analysis. Single-frame iCCD images are obtained with a PCO DiCam Pro camera (1280 × 1024 pixels), with exposure time of 10 ns. All experimental times t are given relative to the trigger time of the gun electrodes. Details of the data reduction and analysis methodologies have been used extensively and reported elsewhere.[37,39,40,44]

B. Setup for merging of two and three plasma jets

Two or three adjacent guns (at the vertices of the hexagonal mounting pattern) are used in the two/three-jet experiments (results of Sec. III), as depicted in Fig. 2. Different gas species (N, Ar, Kr, Xe) are used for the two/three-jet experiments. A side-on perspective of three jets merging with diagnostic positions is shown in Fig. 3. Diagnostic chords are approximately 70° relative to the plane of the image. Note that only five chords of the twelve-chord interferometer are used.

C. Setup for merging of six and seven plasma jets

The gun positions and diagnostic setup for the six/seven-jet experiments (results of Sec. IV) are shown in Fig. 4. All the six/seven-jet results shown are for Ar jets. Interferometer chords (green dots), normal to the image in Fig. 4, intersect the jet-propagation axes

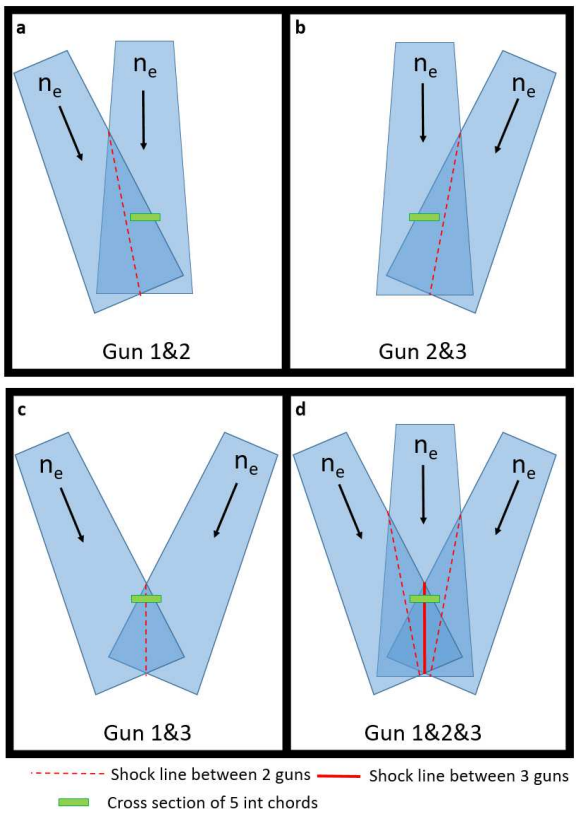

FIG. 2. Setup for results of Sec. III: merging geometry for two- and three-jet merging experiments. The angle is 23.2° between guns 1,2 and 2,3, and 41° between guns 1,3. See Fig. 4 for gun positions.

14.7 cm from chamber center (5.7 cm in the plane of projection). Note that only seven chords of the twelve-chord interferometer are used.

III. EXPERIMENTAL RESULTS: MERGING OF TWO AND THREE PLASMA JETS

The primary new results of this section are the detailed characterizations of the dynamics and shock formation/evolution of two- and three- jet merging (see Fig. 5), substantially augmenting our recent studies that were focused on ion heating for two-jet merging,[43,44] which are based on some of the same experimental campaigns presented here. Firstly, interferometer and spectrometer data are presented to provide space- and time-resolved n_e, T_e, and $\bar{Z}$. Secondly, we discuss and provide an explanation for the observed shock morphology, including quantitative arguments based on the collisionality of the jet merging. All results from Sec. III are for the setups shown in Figs. 2 and 3.

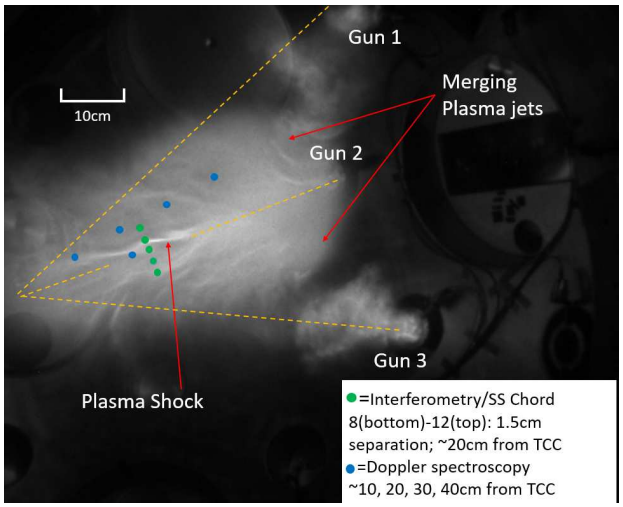

FIG. 3. Setup for results of Sec. III: annotated, side-on visible image (10-ns exposure, $t = 36$ μs) of three merging argon plasma jets. Shown are the locations of five interferometry and survey-spectroscopy viewing chords (green dots) and five high-resolution Doppler spectroscopy chord positions (blue dots). The horizontal row of blue dots intersects the jet-1,2 merge plane.

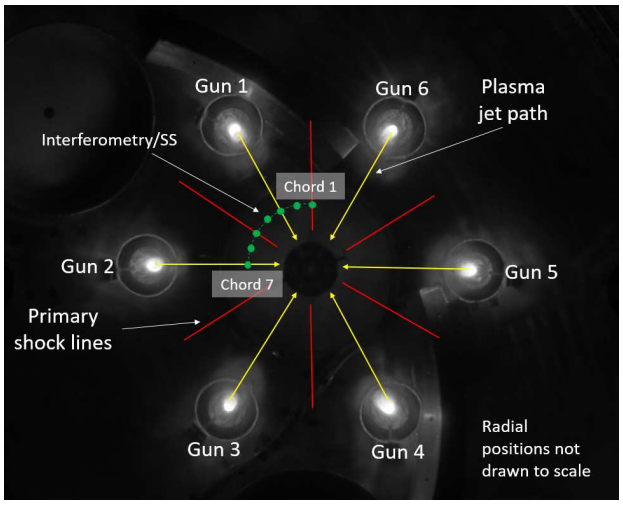

FIG. 4. Setup for results of Sec IV: annotated, end-on visible image (10-ns exposure), showing the inside of the 9-ft.-spherical vacuum chamber, the location of six of the plasma guns, and locations of seven interferometer and survey-spectroscopy viewing chords. The angle between adjacent guns is 23.2°. A seventh gun (not shown here) is installed at the center of the hexagon.

A. Inferring plasma parameters and density jumps upon jet merging

Measurements of n_e are obtained via the five interferometry chords shown in Fig. 3 (green dots). The time-resolved, line-integrated n_e averaged over several shots using Ar jets is compared to synthetic data from SFP-

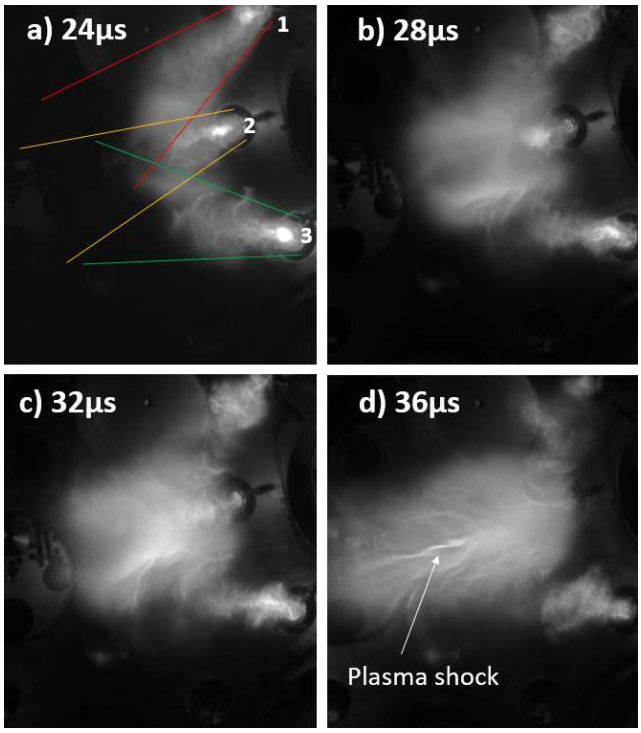

FIG. 5. Visible self-emission images (10-ns exposure) of three-jet merging. (a) Approximate jet-propagation envelopes. (b) and (c) Jets 1,2 and 2,3 have merged. (d) All three jets have merged with a narrow region of intense emission, which we show in this paper to be consistent with a plasma shock.

Max in Fig. 6 (see Fig. 17 in Appendix A for N, Kr, and Xe data). Some degree of symmetry is expected around chord 10 for all gas species. The colors of each trace represent a specific laser chord, with similar colors expected to have similar values, i.e., light blue and dark blue. The higher line-integrated n_e for a particular chord, e.g., chord 10 in Fig. 6, reflects an increase in n_e due to the formation of a plasma shock as the plasma jets merge. This is consistent with previous, detailed oblique plasma-shock studies.[38,39] The lack of symmetry about chord 10, which is along the midplane of jet 1,3 merging as shown in Fig. 3, is due predominantly to $> 20\%$ mass imbalance in the different plasma jets due to variations in the GV injection. The variation is reduced to $< 2\%$ for the results in Sec. IV. The ability to match simulation results to the data was difficult to achieve, requiring customized simulation initial conditions for each jet in an attempt to match the observed asymmetries. Using the initial, experimentally inferred values of jet density, length, temperature, and axial density profile, we still had to make assumptions about free simulation parameters in the velocity gradients, divergence of the jets (although constrained somewhat by iCCD images), and timing jitter.

Individual shots from Fig. 6 (and Fig. 17 of Appendix A) are analyzed to better infer the density jump due to the shock structure. For each shot, ratios are

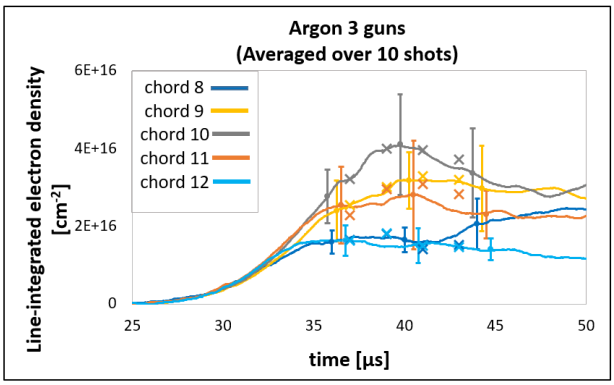

FIG. 6. Interferometer signals versus time for the chord positions shown in Fig. 3 (green dots) for Ar jets. Error bars for select times are one standard deviation of the shot-to-shot variation. Synthetic data from SPFMax simulations (see Sec. III C) for line-integrated n_e are represented by the x's. We expect symmetry around chord 10, with similar signals expected for chords 9 and 11 (yellow and orange) and chords 8 and 12 (dark and light blue).

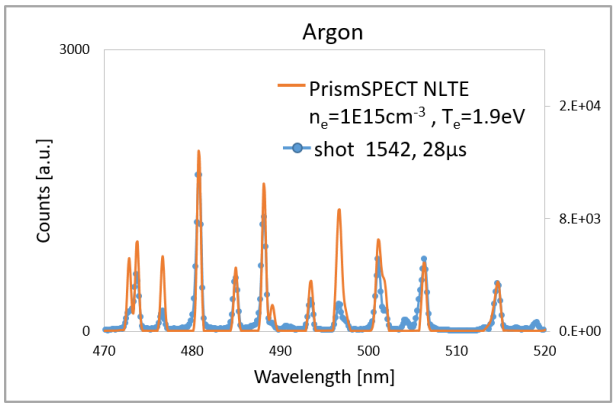

FIG. 7. Comparison of experimental and calculated atomic spectra for three-jet merging for Ar, at the location of chord 10 (the middle green dot in Fig. 3). Inferred n_e and T_e are given in the legend.

taken between chords with the highest and lowest line-integrated densities, with the former assumed to represent post-shock and the latter pre-shock plasma regions. The high-density shock structure is observed to move across interferometry chords in time as observed in the iCCD images. For each species, the maximum ratio between the chords with the highest and lowest line integrated density, and their standard deviation, are also determined. The information is summarized in Table I.

The lengths of the merged jets are estimated by taking the full-width half-maximum of the line-integrated n_e traces. The merged jet lengths are estimated to be 148, 87, 88, and 57 cm for N, Ar, Kr, and Xe, respectively. The long lengths compared to that of individual jets ($<$ 20 cm) are primarily due to speed differences between jets leading to an extended merged-plasma region. Further reductions in individual jet lengths and mass/speed variations across jets are needed; improvements are presented in Appendix B.

To infer T_e and $\bar{Z}$, survey-spectroscopy data is compared to non-local-thermodynamic-equilibrium (non-LTE) calculations of atomic spectra using PrismSPECT,[49] by noting when specific line transitions appear or disappear as a function of n_e and T_e.

TABLE I. Ratio between chords with the highest and lowest line-integrated densities, as a measure of the shock n_e jump for three-jet merging, based on the individual shots used in Figs. 6 and 17.

Gas Species	N	Ar	Kr	Xe
Average	2.9	4.2	6.1	6.6
Standard Dev.	0.8	1.1	1.4	3.1
Maximum	4.6	6.4	8.9	13.6

Values of n_e consistent with interferometry measurements are used in PrismSPECT calculations to bound T_e and $\bar{Z}$. Figure 7 shows the comparison of experimental spectra and PrismSPECT calculations for three-jet merging using Ar (see Fig. 18 in Appendix A for N, Kr, and Xe data). The inferred $T_e \approx$ 1.2–3.2 eV (across all four species) including error bars, which are given in Table II, for $n_e = 10^{15}$ cm^{-3} (this is the estimated density of the post-merged plasma). The PrismSPECT calculations indicate singly and doubly ionized states with $\bar{Z}$ = 0.9–1.9 (across all four species). Interestingly, post-merged plasma jets do not show much spatial nor temporal variation in T_e. There are discrepancies between the experimental and calculated line ratios in Figs. 7 and 18, which may be due to the line-integrated light collection spanning regions of different plasma parameters.

Figure 8 shows comparisons of experimental and calculated spectra among different jet-merging configurations and a single jet for Ar. Across all merging configurations, the spectra do not significantly change, implying similar values of T_e and $\bar{Z}$, but the spectra for a single jet is different. Comparing with PrismSPECT calculations, the single-jet spectra indicates T_e = 1.5 eV and $\bar{Z}$=0.9 for a density of 5×10^{14} cm^{-3} (pre-merged density estimate), while the merged-jet spectra indicates T_e = 1.9 eV and $\bar{Z}$=1.0 for a density of 1×10^{15} cm^{-3}. Similar increases in n_e, T_e, and $\bar{Z}$ for merging versus a single jet are observed for all gas species and summarized in Table II. The increase in T_e and $\bar{Z}$ in merging configurations compared to a single jet was observed in prior experiments,[40] which was attributed to frictional heating of electrons from slowing of the oppositely directed ions. The rate of slowing can be estimated using the ion-electron slowing-down rate. Using the estimated parameters for each species, the slowing-down rate for nitrogen is calculated to be significantly larger (factors of approximately 2–3) than the other three species. If this

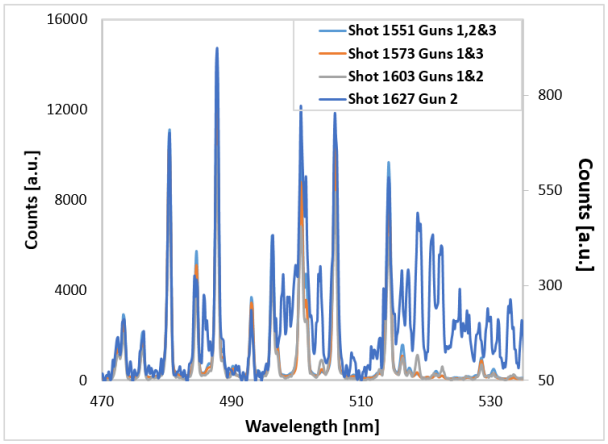

FIG. 8. Measured atomic spectra (chord 10, $t = 36$ μs) for three different argon-jet-merging configurations (shots 1551, 1573, 1603; very similar spectra) and a single jet (shot 1627; very different compared to merging configurations). The values of pre- and post-merge T_e and $\bar{Z}$ are given in Table II.

TABLE II.
Experimentally inferred values of T_e and $\bar{Z}$ for single and merged jets, for four gas species. The merged values are representative of both two- and three-jet merging.

	single jet	merged jets
	$[T_e(\text{eV}),\ \bar{Z}]$	$[T_e(\text{eV}),\ \bar{Z}]$
N	[1.3±0.3, 0.8±0.2]	[2.8±0.4, 1.4±0.4]
Ar	[1.5±0.3, 0.9±0.3]	[1.9±0.5, 1.0±0.1]
Kr	[1.2±0.4, 0.8±0.4]	[1.9±0.5, 1.2±0.3]
Xe	[1.4±0.4, 1.0±0.3]	[1.7±0.5, 1.5±0.4]

is the leading mechanism for increased T_e, then it could explain the larger increase in T_e for nitrogen.

B. Prospect of shockless jet merging

Earlier two-jet merging experiments using mini-railguns on PLX demonstrated oblique plasma-shock formation in highly collisional regimes.[38,39] Simulations of spherical-plasma-liner formation via merging jets in the collisional, hydrodynamic limit showed a "cascade of shocks" as jets merged and during the subsequent liner implosion.[31] More recently, collisional plasma-shock formation was reproduced using coaxial plasma guns,[43,44] but those experiments also showed that jet–jet interpenetration without shock formation could occur in less-collisional regimes.[43,44]

This leads to the idea of deliberately operating in a less-collisional jet-merging regime to avoid shock formation, thereby minimizing the seeding of density perturbations in plasma-liner formation as desired for PJMIF.[44] The three-jet-merging results of this paper point to further constraints. We will show that in these experiments, despite the likelihood that the merging of only jets 1,2 and 2,3 and 1,3 are occurring in an interpenetrating regime, the collisionality is increased to form a shock when all three jets merge.

For these experiments, interferometer data do not show large density jumps associated with a shock front passing through for any of the two-jet configurations shown in Fig. 2. This is supported by two-jet interferometer data discussed later in Figs. 10(b) and (c), where maximum density jumps are < 2. Furthermore, the iCCD images in Figs. 5(b) and (c) show a diffuse bright region at the merge regions between jets 1,2 and 2,3. The diffuse emission morphology was shown previously to correspond to an interpenetrating, shockless jet-merging situation.[40,43,44]

However, despite the two-jet merging leading to shockless, semi-collisional interpenetration, the merging of all three jets leads to a shock, as seen in Fig. 5(d) and the > 2 density jump in Fig. 10(a). Here, we show that the presence of a shock in three-jet merging, despite the absence of shocks in two-jet merging, is due to dynamically increasing T_e and $\bar{Z}$ due to jet merging. This is exacerbated by the presence of impurity titanium, which leads to even higher $\bar{Z}$. We denote this the "Moser effect," which was first observed in head-on jet-merging experiments on PLX;[40] a similar effect has been recently observed in laser-driven experiments.[50]

The presence of titanium, from the inner electrode of the coaxial plasma guns, is evident from side-on survey-spectroscopy data (Fig. 9) taken at the chord-10 position (see Fig. 3). To estimate the fraction of impurities in the plasma jets, vacuum-chamber pressure rise for gas injection only is compared against that with plasma-jet discharges, which presumably ablates some electrode material. This comparison suggests that the plasma jet has 80% injected gas species (in this case Ar) and 20% impurities. The three Ar jets arrive at the chord-10 position at about 27 μs (see Fig. 6). The titanium impurities, Ti II and Ti III, appear around 34 μs, with about 10 μs of leading edge of the jet having little to no measurable impurities. The best-fit PrismSPECT calculations indicate $\bar{Z} = 1.0$ for the data at $t = 30$ μs and $\bar{Z} = 2.0$ for $t = 34$ μs. We estimate that only $\sim 5\%$ of the jet mass is in the leading edge where there is little-to-no titanium. Unfortunately the spectroscopy analysis of impurities was only conducted for argon jets.

Combining all the information on plasma parameters that we have gathered here and elsewhere,[44] we provide quantitative estimates of the collisionality for three-jet merging for both cases of with and hypothetically without impurities. As discussed previously,[39] the ion–ion interpenetration length is

$$L_{ii,s} = \sum_{i'} \frac{v}{4\nu_{ii',s}}, \tag{1}$$

where $\nu_{ii',s}$ is the ion–ion slowing frequency in the fast

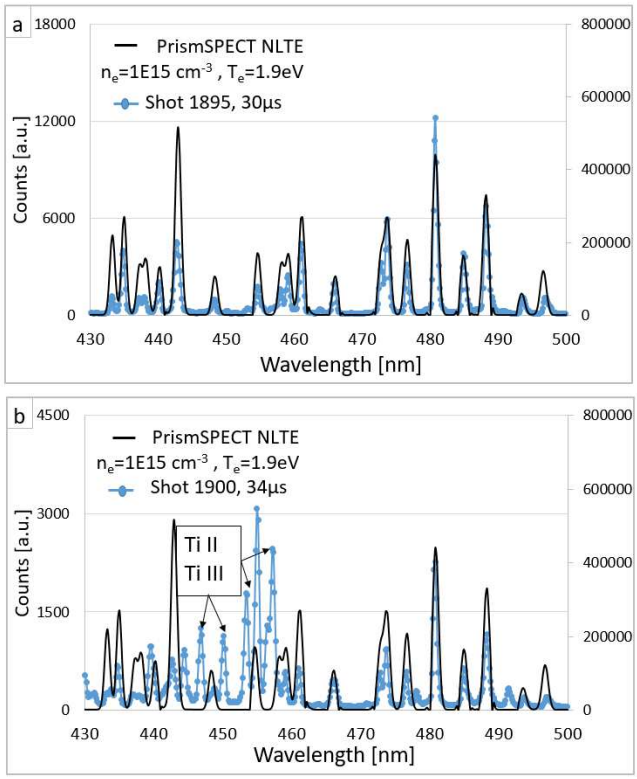

FIG. 9. Survey-spectroscopy data (chord-10 position) for three-jet merging (Ar) and fits to PrismSPECT calculated spectra (no Ti), for (a) leading front of the jet (no Ti) and (b) bulk of the jet (with Ti).

limit ($\gg \nu_{ie,s}$ for the present parameters),[51]

$$\nu_{ii',s} = 9\times10^{-8} n_i' \Lambda_{ii'} \bar{Z}'^2 \bar{Z}^2 \left(\frac{1}{\mu}+\frac{1}{\mu'}\right)\frac{\mu^{1/2}}{\epsilon^{3/2}}, \qquad (2)$$

and $v = 2v_{jet}\sin\theta$ is the relative normal speed between counter-streaming plasma jets, θ is the half angle between jets, n_i is the ion density, $\Lambda_{ii'}$ is the Coulomb logarithm for counter-streaming ions in the presence of warm electrons,[39] μ is the ion/proton mass ratio, and ϵ (eV) is the energy associated with v. In Eq. (1), the factor of 4 is the integral effect of the slowing down,[36] and the summation is over all gas species. Prime and unprimed variables refer to field and test particles, respectively.[51] Table III shows calculated $L_{ii,s}$ for each jet species using averaged plasma parameters. The impurity (Ti) speed is assumed to be the same as for the majority species. The T_e and $\bar{Z}$ are determined from survey spectroscopy for post-merging of jets, with the same values assumed for Ti across all jet species, while n_e is from interferometry. The half-angle $\theta = 20.5°$ between jets 1,3 is used in these estimates. Two estimations of $L_{ii,s}$ are calculated for the 80%/20% mixtures, i.e., with the majority and impurity species each treated as the test particle, respectively. For both cases, $L_{ii,s}$ values are summed over both field ion species, as indicated in Eq. (1). To be in a highly collisional limit with shock formation, $L_{ii,s}$ should be $\ll 30$ cm (jet system size, from the iCCD images). Our calculations show that using the parameters from Table II (for jets with no impurities) would result in substantial interpenetration. This is consistent with the lack of shock structure observed in the iCCD images and the interferometry chords for the merging of jets 1,3. However, as seen in Table III, the merging of all three jets leads to an increase in T_e and $\bar{Z}$ compared to Table II. This, along with the presence of Ti impurities with even higher $\bar{Z}$, leads to an increase in collisionality and reduction in $L_{ii,s}$ and therefore the formation of a shock along the center line of the three jets, as observed in Fig. 5(d).

To summarize the primary points of this subsection, it is possible to have semi-collisional, interpenetrating, shockless jet merging, which may be desirable for plasma-liner formation to minimize the amplitude of density non-uniformities. However, jet merging leads to slightly elevated T_e and $\bar{Z}$ that is further exacerbated by the presence of jet impurities, like Ti, that tend to have even higher $\bar{Z}$. Because collisionality $\sim \bar{Z}^4$, it is easy to transition into a regime with shock formation, i.e., "Moser effect," for multiple-jet merging in the presence of impurities. This points to a need to further reduce the impurity content in the plasma jets to enable shockless jet merging as an option for plasma-liner formation.

C. Liner Mach-number degradation

Maintaining a high liner Mach number M to enable efficient target compression has been identified as important for the viability of PJMIF.[17,21] The recent, related results on shock ion heating in two-jet merging experiments showed that ion heating to tens of eV occurs upon jet merging for cases with and without shock formation.[44] This degrades M, but due to very fast cooling of the ions on the few-eV electrons over a several-μs timescale, M should quickly increase. In this work, we estimate M and its evolution using the previously reported high-resolution Doppler-spectroscopy data (providing ion temperature T_i)[43,44] and the interferometer/survey-spectroscopy data of this paper. We use the data to benchmark hydrodynamic simulations of jet-merging using the three-dimensional SPFMax smooth-particle hydrodynamics (SPH) code.[45] Simulations of fully spherical plasma-liner formation and implosion, benchmarked to our localized jet-merging experimental data, show that the liner-averaged M remains high even with the transient localized reduction due to shock heating.

Doppler-spectroscopy data, providing time- and space-resolved T_i,[43,44] was obtained at the positions of the blue dots in Fig. 3. Along with T_e and $\bar{Z}$ data presented in this paper, the time- and space-resolved $M = v_{\rm jet}/C_s$ is calculated in the jet-merging and shock regions, where $C_s = (\gamma p/\rho)^{1/2} = [\gamma(\bar{Z}T_e + T_i)/m_i]^{1/2}$. We use the gas sound speed definition due to the very high colli-

TABLE III. Collisionality of jet merging is evaluated based on Eqs. (1) and (2), using $\theta = 20.5^\circ$ corresponding to the half-angle between jets 1,3. Results are shown assuming 100% majority-species jets (top half of table) and an 80%/20% mixture of majority-species/Ti jets (bottom half of table). The two values of $L_{ii,s}$ shown for the 80%/20% mixtures are for majority and Ti ions as the test particles, respectively.

Species	N	Ar	Kr	Xe
v (km/s)	36.5	29.4	39.8	19.2
n_e ($10^{14} cm^{-3}$)	3.0±0.3	2.9±0.4	3.3±2.0	2.6±0.3
T_e(eV)	2.8±0.4	1.9±0.4	1.9±0.5	1.7±0.5
$\bar{Z}$	1.4±0.4	1.0±0.1	1.2±0.3	1.5±0.4
$L_{ii,s}$(cm)	1.5	18.0	109.0	8.0
Species	80%N/20%Ti	80%Ar/20%Ti	80%Kr/20%Ti	80%Xe/20%Ti
v (km/s)	36.5	29.4	39.8	19.2
n_e ($10^{14} cm^{-3}$)	2.4/0.6±0.2/0.1	2.4/0.5±0.3/0.1	2.6/0.7±1.6/0.4	2.1/0.5±0.2/0.1
T_e(eV)	2.8/1.4±0.4/0.2	1.9/1.4 ±0.4/0.2	1.9/1.4 ±0.5/0.2	1.7/1.4±0.5/0.2
$\bar{Z}$	1.4/2.0±0.4/0.4	1.9/2.0±0.1/0.4	1.2/2.0±0.3/0.4	1.5/2.0±0.4/0.4
$L_{ii',s}$(cm)	1.3/3.0	8.8/5.0	50.0/2.6	4.7/0.4

sionality, which invalidates the isothermal assumption for electrons. Adiabatic index $\gamma = 5/3$ is assumed due to the unconstrained three-dimensional motion of both electrons and ions in our unmagnetized plasmas (note: γ can be $< 5/3$ for low charge states of Ar, Kr, Xe,[23] so we may be underestimating M). Figure 10 shows side-on interferometry and inferred M using Doppler-spectroscopy measurements of T_i at approximately 20 cm from chamber center (see Fig. 3) for three different argon jet-merging configurations. The interferometry traces shown in Fig. 10(a) and (b) cross the region where the plasma jets merge and plasma shocks can form. Figure 10(a) shows a large ratio (> 2) of line-integrated n_e between the chords with the highest and lowest values, consistent with the presence of a shock, while Fig. 10(b) shows a much smaller ratio (< 2). For the three-jet case [Fig. 10(a)], the jet merging leads to collisional ion heating, resulting in a low M, followed by subsequent cooling of the ions through collisional equilibration with the cool electrons, which allows M to increase back up to nearly 7. For the two-jet case at larger angle [Fig. 10(b)], ion heating is observed; however, the lower density inhibits radiative cooling and results in a lower M. For the two-jet case at smaller angle [Fig. 10(c)], the collisional ion shock heating leads to a low M followed by cooling that leads to a high Mach number.

Hydrodynamic simulations using the SPH code SPFMax[45] are conducted and benchmarked against the two- and three-jet merging data in this paper. SPFMax and its predecessor codes have been used extensively for both one- and three-dimensional modeling of imploding plasma liners.[28,30] Figure 11 presents results for two-jet argon merging compared to simulations using SPFMax, showing (1) experimentally inferred M values within the jet-merging region of jets 1,2 (black dots); (2) simulated local values of M at the region of merging (red line); and (3) simulated spherical-liner-averaged M (blue line), indicating that the liner-averaged M remains $\gtrsim 10$ despite the localized value in the jet-merging region falling well below 10. The experimentally inferred M values use T_i measurements from the blue dots along the jet 1,2 midplane shown in Fig. 3. The ability for the global M to remain > 10 and the localized M to rise back to $\gtrsim 10$ is important for the viability of the PJMIF concept because degradation in M would lead to an increase in liner spreading, which would degrade the liner's ability to compress a plasma target to fusion-relevant conditions.[21]

IV. EXPERIMENTAL RESULTS: MERGING OF SIX AND SEVEN PLASMA JETS WITH IMPROVED JET-TO-JET MASS BALANCE

The primary objectives of this section are to experimentally characterize the structure of the section of a plasma liner formed by six and seven hypersonic merging plasma jets (see Fig. 4), and to demonstrate improved mirror symmetry in the liner structure about the jet-propagation axes due to the improved jet-to-jet mass balance compared to earlier work.[41] Experimental evidence for the improved jet-to-jet balance, achieved by upgraded GVs and fine-tuned series (ballast) impedances of the GVs, is presented in Appendix B. Figure 12 shows end-on images of the merging of six and seven plasma jets. Primary shocks (defined here as the oblique formation of plasma shocks and appearing as radial spokes) are observed to form between adjacent jets[43,44], for both six- and seven-jet cases by ≈26 μs [Figs. 12(b) and (f)]. The seven-gun configuration also forms primary shocks [hexagonal pattern, Fig. 12(f)] between the six outer jets and the seventh jet. The initially merged plasmas from adjacent jets appear to all merge and form a secondary shock (defined here as the merging of post-shock plasma regions) near the center, pointing out of the page

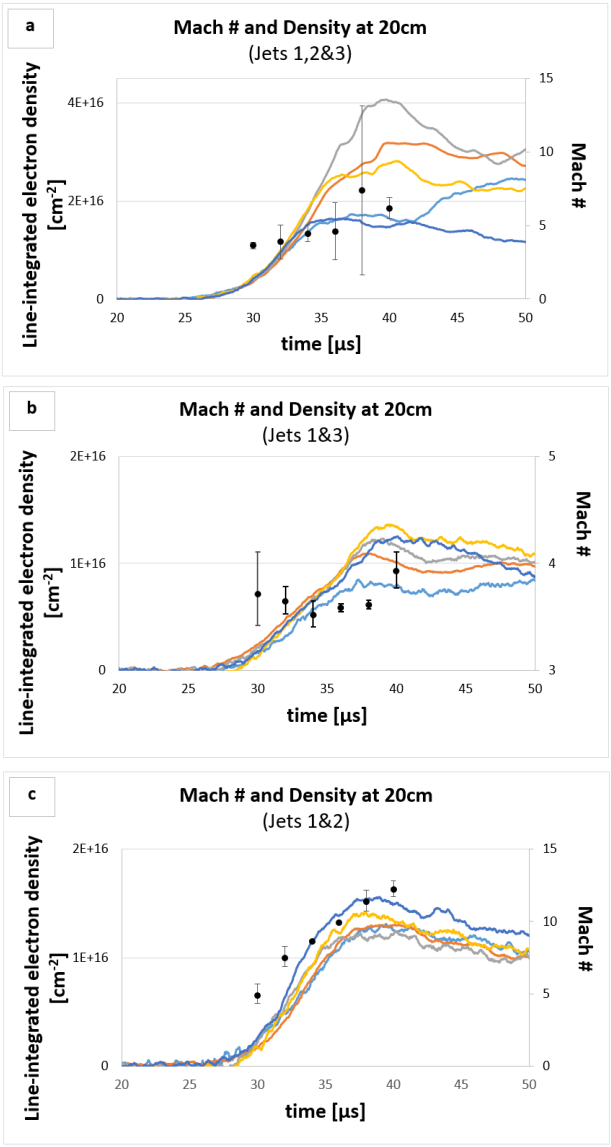

FIG. 10. Line-integrated n_e (colored lines) and experimentally inferred values of M (black dots) for merging of jets (a) 1,2,3, (b) 1,3, and (c) 1,2. The data are all taken at 20 cm from chamber center, at the jet-2 propagation axis for (a) and (b) and the jet 1,2 midplane for (c) (see Fig. 3 for positions). Colors correspond to the chord numbers shown in the legends of Fig. 6.

[Figs. 12(d) and (h)]. In this section, we present interferometry data to characterize time- and space-resolved n_e and T_e associated with the jet merging. Comparisons are made with synthetic data from SPFMax[45] three-dimensional hydrodynamic simulations. Previously published FronTier hydrodynamic simulations provide information on the influence of jet-to-jet variations (in both mass and timing) on the structure and quality of plasma-liner formation,[46] showing good agreement with the images in Fig. 12 for mass variations of $< 10\%$ and timing variations of ≤ 100 ns.

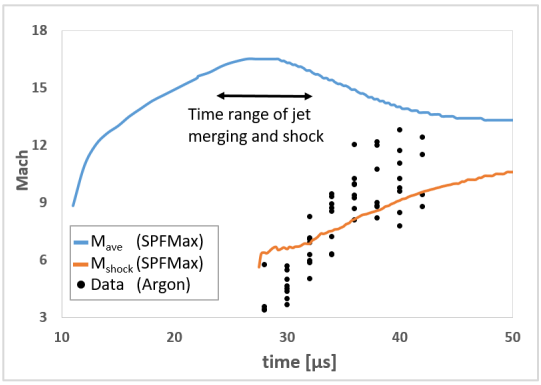

FIG. 11. Mach number versus time: black circles and orange line are the experimentally inferred and simulated values, respectively, within a two-jet merging region (guns 1,2). Solid blue line is the simulated, liner-averaged Mach number from the same spherical simulation, showing that the liner-average value remains above ~ 10 even while the localized value within the jet-merging region falls below 10.

A. Spatial density uniformity

With reasonably good jet-to-jet balance, it is expected that the density profile along the interferometer chord positions will exhibit mirror symmetry about chords 3 and 5, i.e., similar values for chords 1 and 5, chords 2, 4, and 6, and chords 3 and 7 (see Fig. 4). This was not observed in earlier six-jet merging experiments due to poor jet-to-jet balance.[41] The new data presented here shows a significant improvement in the mirror symmetry of the density profile about chords 3 and 5, and a gentler density gradient compared to those in the synthetic data from from both SPFMax[45] and FronTier.[46]

The seven-chord interferometer provides time- and space-resolved, line-integrated n_e at the positions shown in Fig. 4 for six-jet merging. Figure 13 shows the interferometry data compared to synthetic data from SPFMax at different times, both before (left column) and after the GV and ballast upgrades (right column), which are described in Appendix B. The perfect mirror symmetry about chords 3 and 5 is of course seen in the synthetic data, and a substantial improvement is seen in the experimental data. The results obtained prior to the GV/ballast upgrade [Fig. 13(a)–(d)] show unbalanced merging of six jets as indicated by the systematically low line-integrated n_e measured in chords 5, 6, and 7. The results obtained after the upgrade [Fig. 13(e)–(h)] show a more-balanced merging of the plasma jets with improved mirror symmetry about chords 3 and 5. However, the symmetry is not perfect and is likely due to the timing and velocity jitter discussed earlier. Nevertheless, better agreement is now achieved between experimental and synthetic SPFMax data.

To further quantify the density non-uniformity for a single shot, individual shots are analyzed from six-jet merging experiments before and after the GV/ballast up-

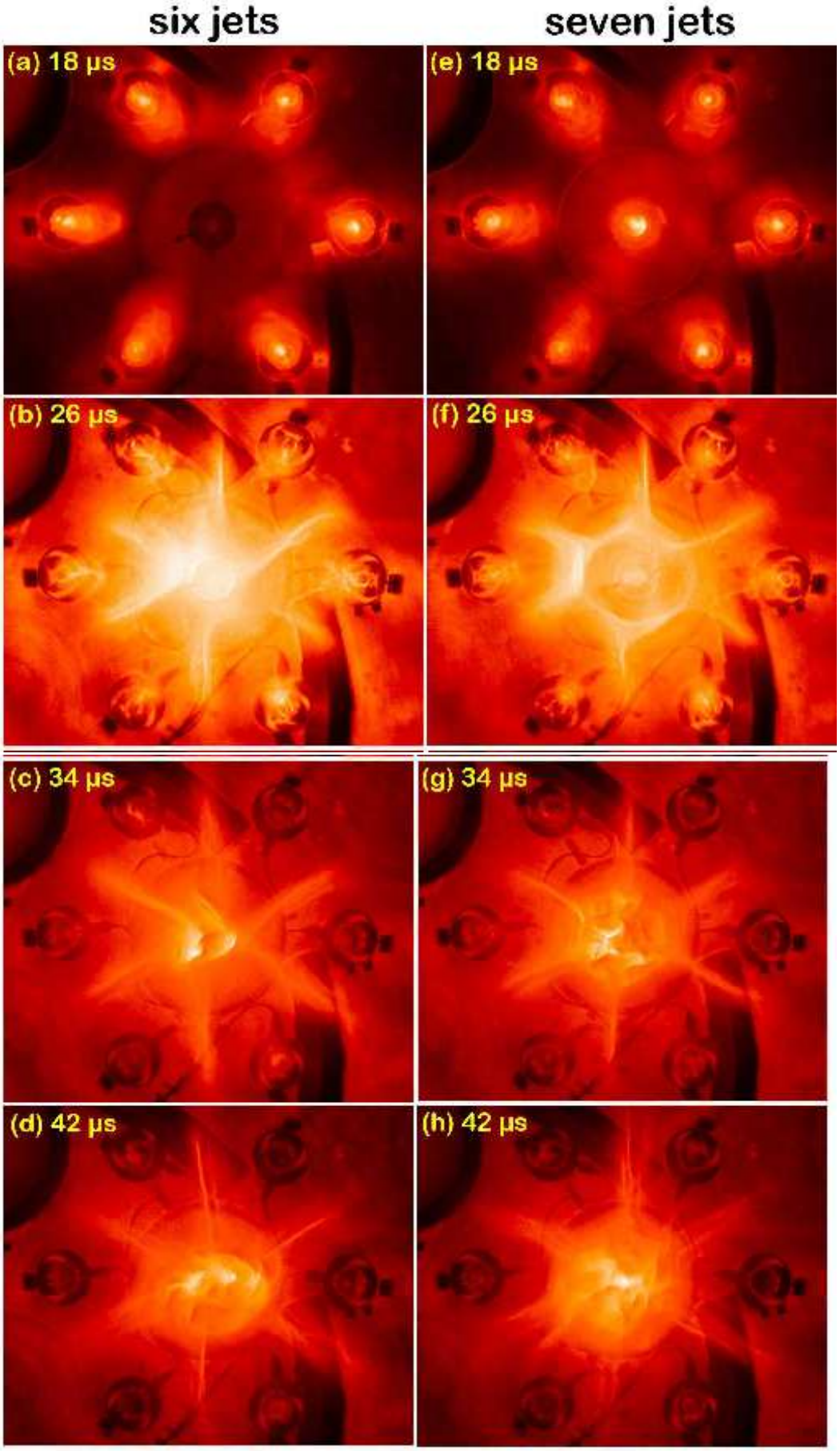

FIG. 12. End-on, self-emission visible images (10-ns exposure, false color) of the merging of six and seven argon plasma jets.

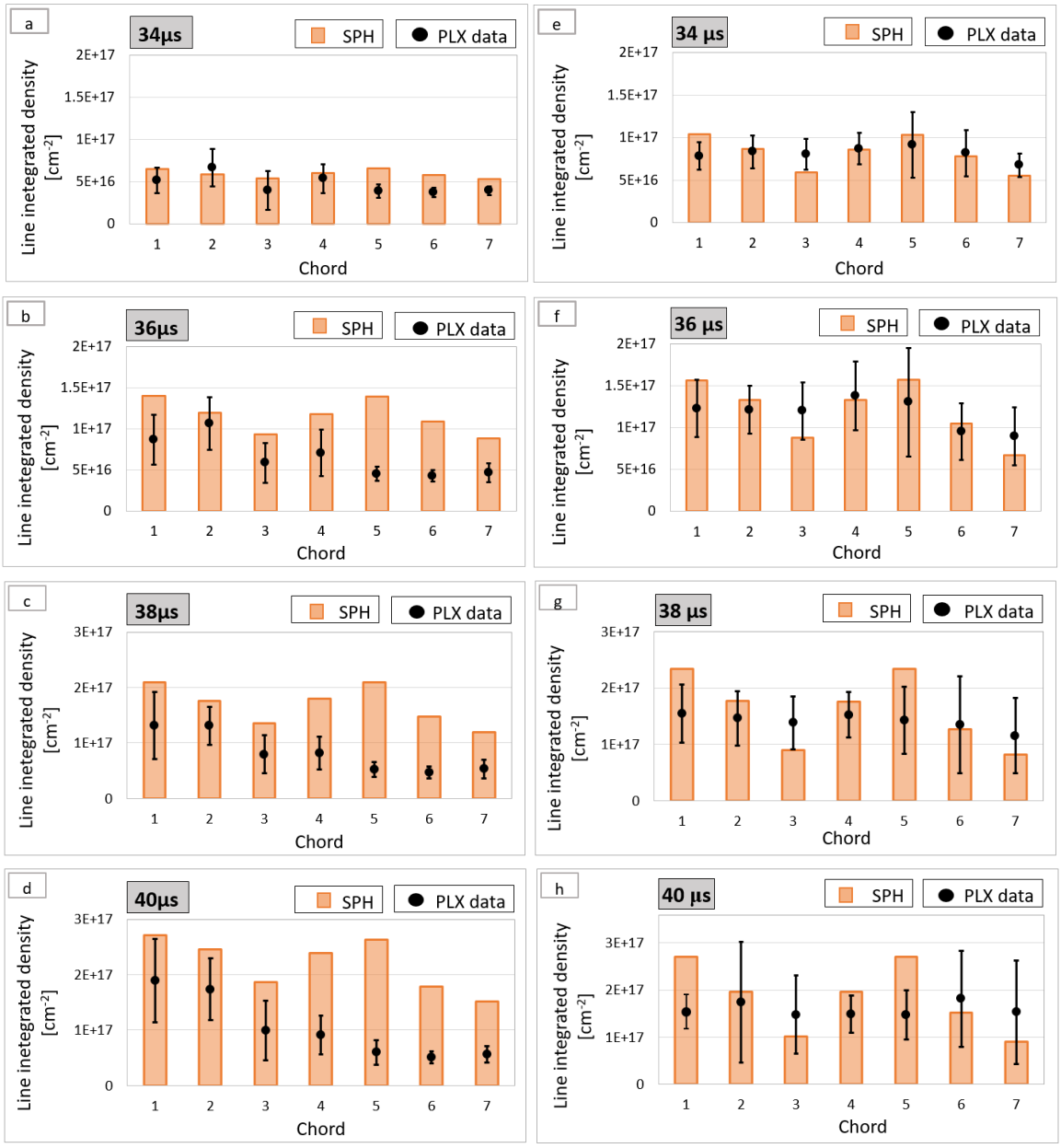

FIG. 13. Experimental and synthetic SPFMax[45] data (dots and bars, respectively) for line-integrated n_e from the interferometer chord positions shown in Fig. 4. Panels (a)–(d) are prior to and (e)–(h) are after GV/ballast upgrades described in Appendix B. Experimental data are averaged over ten shots; the error bars represent one standard deviation of the shot-to-shot variation.

grades. Figure 14 shows that the variation across interferometer chords for individual shots is reduced after the GV/ballast upgrades, with standard deviations across chords falling from 0.4–1.2 $\times$ 10^{17} cm^{-2} before the upgrades to 2–7$\times$$10^{16}$ cm^{-2} after the upgrades. While continued refinements to the jet-to-jet balance will further improve the liner density uniformity, there will be a minimum level of liner non-uniformity from the jet-merging dynamics, as presented and discussed in Sec. III.

B. Constancy of electron temperature in space and time

Knowledge of space- and time-resolved T_e is important for characterizing a section of a spherically imploding plasma liner. It affects the mean-charge state $\bar{Z}$, which has a strong influence on inter-jet collisionality through a $\bar{Z}^4$ dependence [see Eq. (2)], and it affects the electrical resistivity $\sim T_e^{-3/2}$, which affects the eventual magnetic-diffusion dynamics when the liner compresses a magnetized plasma target.

Survey-spectroscopy data (Fig. 15), along with n_e from

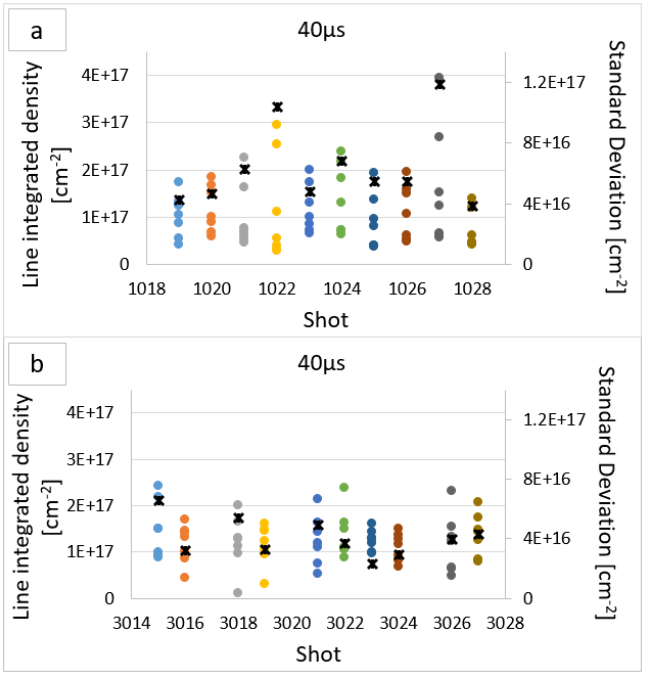

FIG. 14. Line-integrated n_e ($t = 40$ μs) from all seven interferometer chords (colored dots) are plotted versus individual shot numbers from experiments (a) before and (b) after the GV/ballast upgrades. Standard deviation across chords is given by the black x's (right-hand y-axis).

interferometry and comparisons with PrismSPECT[49] calculations, are used to estimate $T_e \approx 1.7$ eV and $\bar{Z} \approx 1.0$ (for $n_e = 10^{15}$ cm^{-3}) along the interferometer chord positions shown in Fig. 4. The results indicate very little variation over different chord positions and times, suggesting fairly uniform T_e in the six-jet merging experiments.

C. Morphology change by adding a seventh plasma jet

Adding a seventh gun (to the middle of the hexagonal vertices where the six guns are mounted, see Fig. 4) provides the opportunity to explore the qualitative change in the structure of the liner section that is formed. This also helps further constrain and benchmark the simulations. Figure 12 shows the different morphology of the six- versus seven-jet merging cases. As discussed briefly earlier in the paper, a new hexagonal pattern of merging shocks appears due to the presence of the seventh jet. Unfortunately, interferometry was not possible for these experiments because the seventh gun uses the same chamber port as the interferometer launch optics.

Side-on images show a dramatic change in shock structures with the introduction of the seventh jet, as seen in Fig. 16. The six-jet case shows a sharp secondary shock formed by the merging of the primary shocks along the symmetry axis of the six jets. The seven-jet case shows

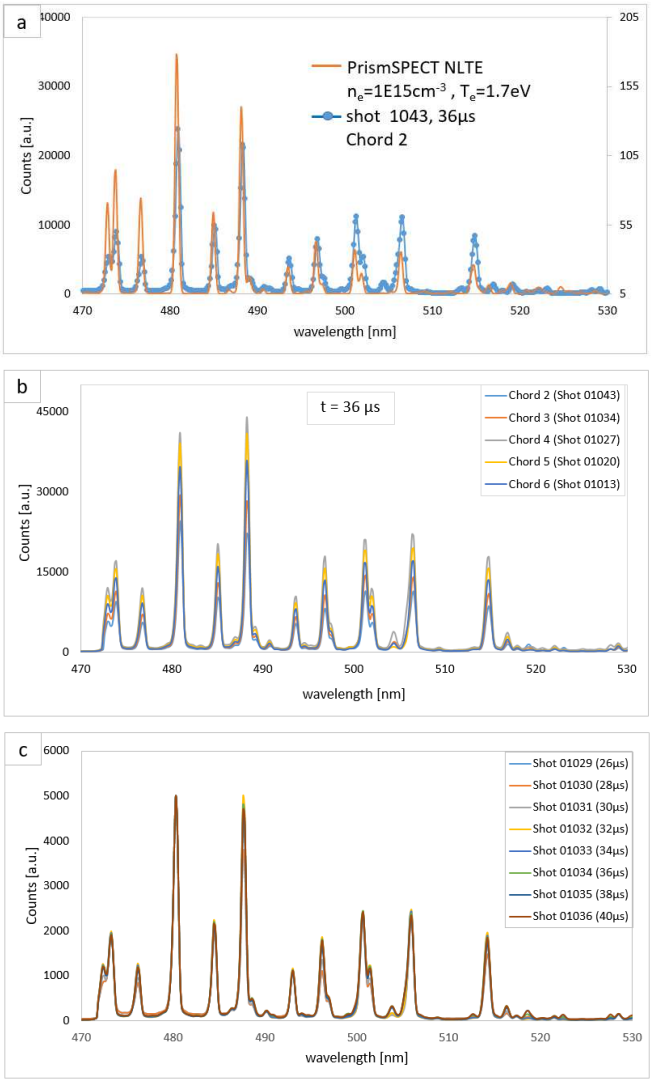

FIG. 15. Survey-spectroscopy data for the chord positions and times shown in the plot legends, showing that the spectra (corresponding to $T_e \approx 1.7$ eV and $\bar{Z} \approx 1.0$ based on comparisons with PrismSPECT calculations) are largely unchanged over different positions and times.

what appears to be several propagating primary shocks, presumably associated with the hexagonal pattern seen in Fig. 12(g). The collisional merging of the six jets with the inner seventh jet modifies the propagation of the six jets as well as the six primary shocks, such that the secondary shock does not form at the same time and position as for the six-jet case. Lineouts of the square root of image intensity across the merged structures are shown in Fig. 16(c). Assuming that T_e is spatially uniform (as shown earlier in the paper), lineouts are representative of the density profile. The seven-jet case shows a much more uniform profile than the six-jet case, showing that gun positioning and merging angles may be a way to optimize the liner uniformity.

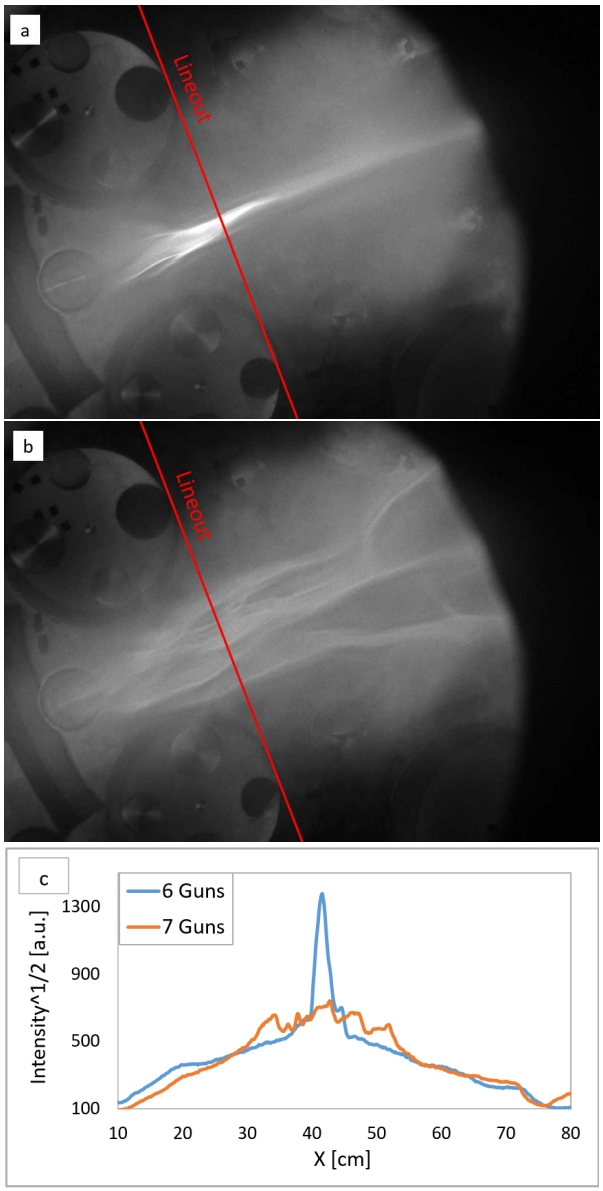

FIG. 16. Side-on, self-emission iCCD images (10-ns exposure, $t = 34$ μs) of (a) six- and (b) seven-jet merging. (c) Lineouts of the square root of the intensity from both images at approximately 20 cm from chamber center.

V. SUMMARY AND CONCLUSIONS

In this paper, we report comprehensive experimental results for the merging of multiple hypersonic jets to form a section of a spherically imploding plasma liner. This is a first major step toward developing plasma liners as a standoff driver for MIF, based on the PJMIF concept.

The first experimental campaign (Sec. III) reported in this paper focused on the merging of two and three hypersonic plasma jets, as the most fundamental building block of plasma-liner formation, to study and characterize plasma-shock formation, spatial density nonuniformities, and liner Mach-number degradation. For plasma jets merging at larger half-angles (20.5°), the merged plasma is more uniform due to the large interpenetration of the plasma jets and the softening or outright elimination of shock formation. For plasma jets merging at smaller half-angles (11.6°), the merged plasma has larger density gradients due to the decrease in inter-jet interpenetration lengths, leading to plasma-shock formation. Jet merging is shown to slightly increase T_e and $\bar{Z}$, leading to an increase in collisionality. This effect, excacerbated by the higher $\bar{Z}$ of titanium impurities, increases collisionality in the merging process, resulting in shock formation and density non-uniformities upon three-jet merging. Upon jet merging, the Mach number degrades to about 4 due to shock heating of the ions but relaxes back to about 12 after $\sim$10 μs due to ion-electron equilibration. Mach-number degradation does not appear to be a serious issue in this parameter space. However, the formation of plasma shocks upon jet merging may pose an eventual threat to the uniformity of magnetized target compression. Obtaining this data is an important first step toward addressing the key question of what asymmetry is tolerable for PJMIF, where the number of jets, as well as their speed, merging angles, and axial profiles, all must be optimized to minimize liner non-uniformity.

The second experimental campaign (Sec. IV) reported in this paper studied and characterized the formation of a section of a spherically imploding plasma liner formed by six and seven plasma jets. Upgraded GVs and a ballasting system were employed to achieve a significantly improved jet-to-jet mass balance of $< 2\%$ (see Appendix B) compared to earlier work[41] and the results of Sec. III. The improvements lead to a more balanced merging of six and seven plasma jets, which are also seen in benchmarked simulations from SPFMax and previously published results from FronTier.[46] The uniformity of the merging process appears to be improved with the addition of a seventh gun in the middle of the six guns. Despite these improvements, interferometry measurements show appreciable shot-to-shot variations in line-integrated electron densities, as well as imperfect mirror symmetry about the symmetry axes. These effects could, eventually, provide a seed for the Rayleigh-Taylor instability that lead to degraded compression of a magnetized plasma target. Continued progress is necessary to reduce the timing jitter (simulations[46] suggest the need for $\leq$100 ns for fusion relevance), the initial plasma-jet length, jet-to-jet velocity balance, and a reduction in shot-to-shot variations.

Further gun upgrades have been implemented since this work, with many of the new guns already mounted on the PLX chamber, to improve on the aforementioned parameters and improve on gun robustness and maintainability. The latest guns will be used in upcoming 18- and 36-gun experiments to form hemispherical and fully spherical imploding plasma liners, respectively. The goal of future experiments should include tuning the plasma-jet merging parameters, including reduction of impurities, to optimize the collisionality parameters such that

the liner density is high enough to provide ion cooling with the surrounding electrons, yet have increased inter-jet penetration to soften or eliminate shock formation. The experimental data presented in this paper are being utilized to benchmark multi-physics models and simulations to guide us in the optimization and design of future experiments.

ACKNOWLEDGMENTS

This work was supported by the Advanced Research Projects Agency–Energy (ARPA-E) of the U.S. Department of Energy (DOE) under contract no. DE-AC52-06NA25396 and cooperative agreement no. DE-AR0000566. HyperJet Fusion Corporation acknowledges the support of Strong Atomics. Original construction and operation of the PLX facility at LANL and earlier development of contoured-gap coaxial plasma guns by HyperV Technologies Corp. (both prior to 2012) were supported by the DOE Office of Science, Fusion Energy Sciences. The data that support the findings of this study are available from the corresponding author upon reasonable request.

Appendix A: Additional data from merging of two and three jets (N, Kr, Xe)

This appendix provides N, Kr, and Xe data, shown in Figs. 17 and 18, supplementing the Ar data shown in Figs. 6 and 7, respectively. See the discussion in Sec. III A.

Appendix B: Improved jet-to-jet balance

The results presented in Sec. IV are based on improved jet-to-jet balance achieved via upgraded GVs and fine-tuned series (ballast) GV impedances. This appendix presents detailed experimental characterization of the improved jet-to-jet balance.

The first six-jet merging experiments on PLX revealed that jet-to-jet mass imbalance ($\gtrsim$ 20% variation across jets) degraded the expected mirror symmetry in density profiles and merging morphology about the jet-propagation axes.[41] Thus, we made significant improvements to the GVs in the plasma guns to reduce the mass variation among jets. The earlier generation of GVs consisted of an in-line plenum, magnetic coils, a flyer plate, and eight metal springs. The flyer plate rests on the eight uncompressed springs. When the GV coils are pulsed with a 10-kV capacitor bank, magnetic pressure pushes the flyer plate against the springs, compressing them far enough to allow the flyer plate to be pushed below gas-inlet holes at the rear of the gun and letting in pressurized gas. In the new GVs, a modified plenum increases precision in the plenum volume. It also increases the

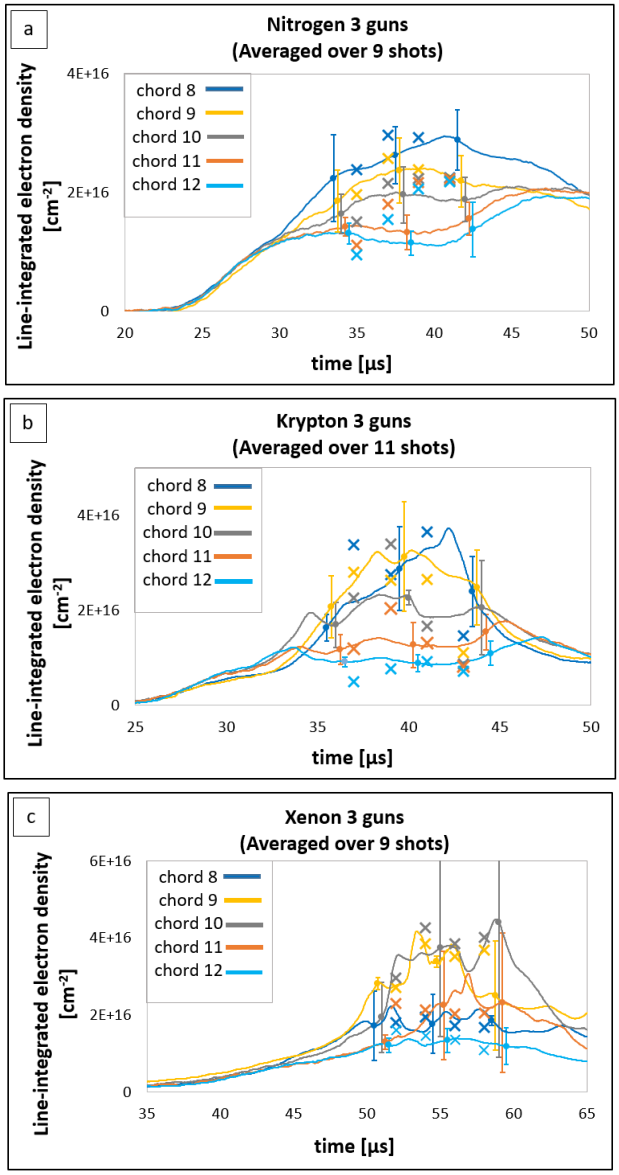

FIG. 17. Interferometer signals versus time for the chord positions shown in Fig. 3 (green dots) for (a) N, (b) Kr, and (c) Xe jets. See Sec. III A and the caption of Fig. 6.

volume, now with an annular profile and a smaller cross-sectional area. This allows higher plenum pressures and larger dispensed masses. Previous GVs applied pressure to the entire flyer plate, whereas the new GV applies annular pressure to the outer rim of the flyer plate. The flyer plate now has an additional fin to direct gas flow towards the inlet holes to the gun breech rather than towards the center of the plate.

However, even with the improved GV design, further fine tuning was still required especially because all the GVs are driven in parallel by a single capacitor bank. The fine tuning is enabled via a ballasting system that allows for adjusting the inductances and resistances in series with each GV to control the split of electrical cur-

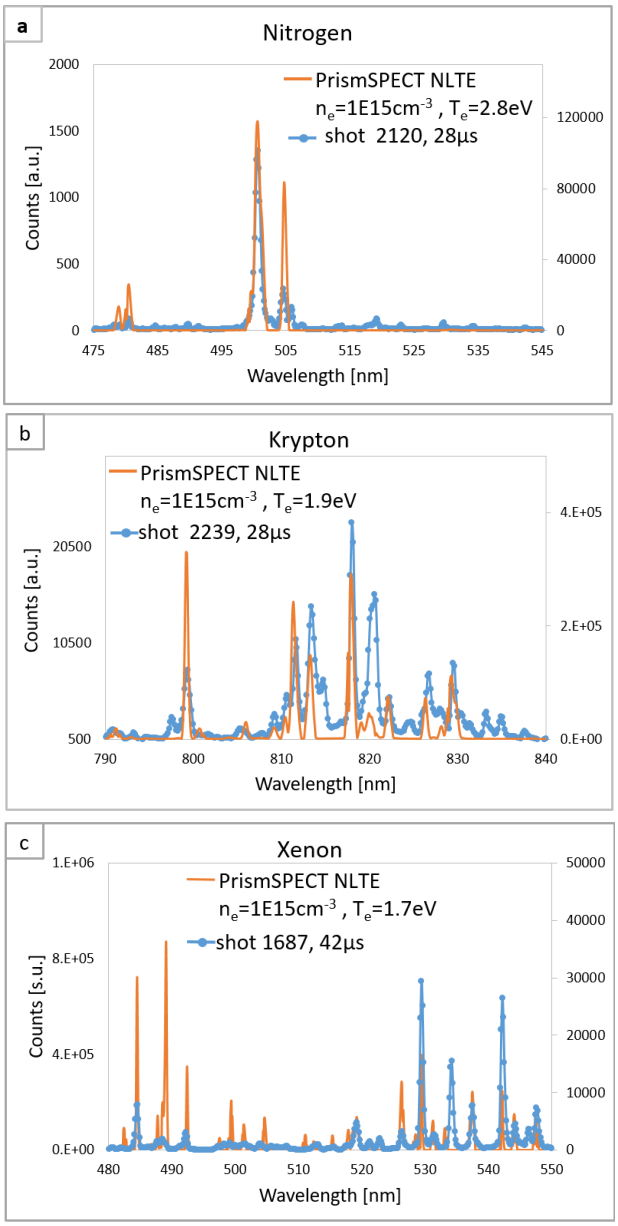

FIG. 18. Comparison of experimental and calculated atomic spectra for three-jet merging for N, Kr, and Xe, at the location of chord 10 (the middle green dot in Fig. 3). Inferred n_e and T_e are given in the legends of each panel. See Sec. III A.

rent delivered to each GV. The fine-tuning sequence is as follows. Gas lines are disconnected from all but one GV and evacuated. The mass injection by the one GV is determined by monitoring the increase in vacuum chamber pressure when all GVs are pulsed. The increase in chamber pressure is determined using an MKS Instruments model 626C.1TLF baratron pressure gauge. The ballast inductance and resistance is adjusted to arrive at an injected mass of 4 mg. This process is repeated for each different GV. Another iteration or two through all GVs is sometimes needed. Using the modified GVs followed by

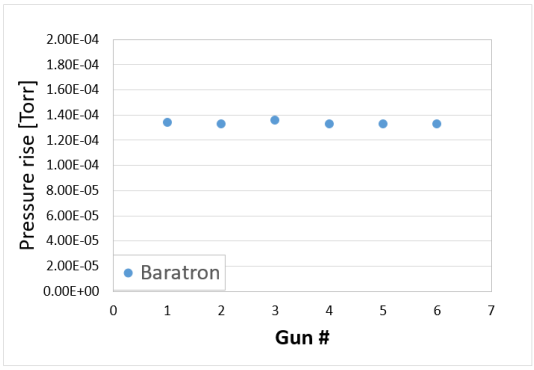

FIG. 19. Chamber pressure rise measured by a baratron pressure gauge for gas injection from each of six plasma guns with upgraded GVs, after fine tuning of ballast inductances and resistances in series with each GV. Results show 1.7% standard deviation in mass injected across six guns.

the tuning of ballast inductances and resistances results in $< 2\%$ variation in the injected mass across all guns, as shown in Fig. 19.

The improved synchronicity of initial jet propagation across all jets is verified via photodiode data (Fig. 20) of the jet propagation as it exits the gun muzzle. Each gun has two photodiode views, separated by 2 cm, transverse to the jet-propagation axis near the exit of the gun nozzle (see Fig. 1). The timing jitter for the six guns is determined by measuring the spread in the photodiode signals. The arrival time of a jet is taken to be the time that photodiode signal reaches half its maximum. Data is analyzed for ten shots, showing an average variation in the arrival time of 610 ns with a standard deviation of 200 ns. Figure 20 shows photodiode traces before and after the GV/ballast improvements. Shot-to-shot jitter in the injected mass now sets the lower bound in the timing variation across jets. End-on imaging of six- and seven-jet merging (e.g., Fig. 12) quickly alerts us if one of the guns is firing with mismatched mass and/or timing.

The photodiode data are also use to determine the velocity and length of the jets (Fig. 21). The velocity is determined from the difference in arrival times of the two photodiode signals for each gun. The length is from the full-width, half-maximum of the photodiode signals. The jet velocities are between 25 and 55 km/s, with the jet from gun three being relatively fast and from gun six being relatively slow. The lengths of the plasma jet upon exiting the nozzle are in the range 7–20 cm. The variations in timing, velocity, and jet length across the guns, as well as from shot-to-shot jitter, show that continued engineering improvements in the gun are needed.

[1]I. R. Lindemuth and R. C. Kirkpatrick, Nucl. Fusion **23**, 263 (1983).
[2]R. C. Kirkpatrick, I. R. Lindemuth, and M. S. Ward, Fus. Tech. **27**, 201 (1995).
[3]I. R. Lindemuth, Phys. Plasmas **22**, 122712 (2015).
[4]G. A. Wurden, S. C. Hsu, T. P. Intrator, T. C. Grabowski, J. H. Degnan, M. Domonkos, P. J. Turchi, E. M. Campbell, D. B.

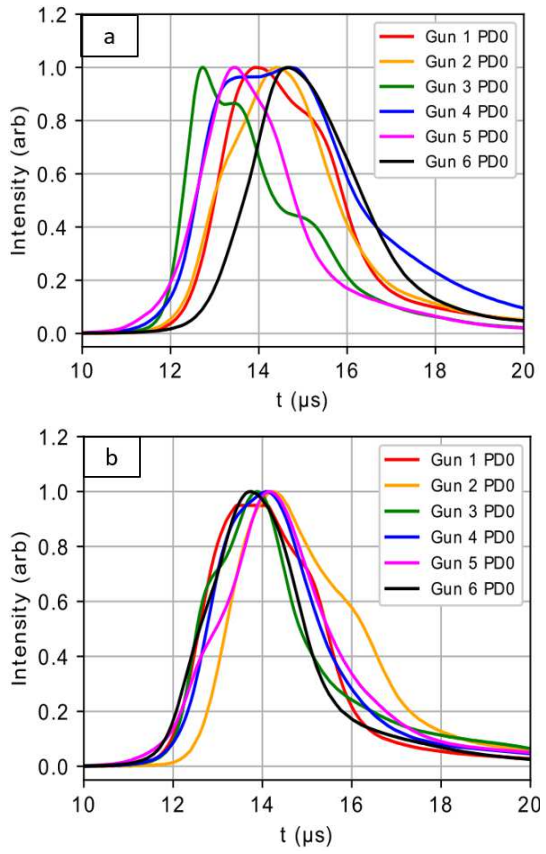

FIG. 20. Photodiode (PD) traces of six jets at the exit of their gun nozzles (see Fig. 1 for photodiode viewing chords) for the upgraded GVs, (a) before and (b) after fine tuning of ballast inductances and resistances.

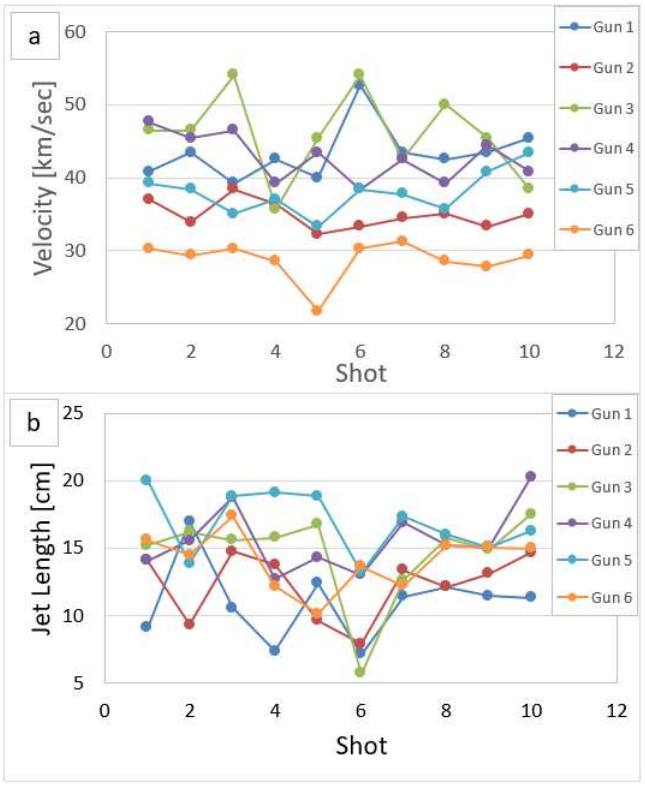

FIG. 21. Jet velocities and lengths from all six plasma guns with upgraded GVs, inferred from photodiode data.

Sinars, M. C. Herrmann, R. Betti, B. S. Bauer, I. R. Lindemuth, R. E. Siemon, R. L. Miller, M. Laberge, and M. Delage, J. Fusion Energy **35**, 69 (2016).

[5] P. J. Turchi, A. L. Cooper, R. D. Ford, D. J. Jenkins, and R. L. Burton, in *Megagauss Physics and Technology*, edited by P. J. Turchi (Plenum, New York, 1980) p. 375.

[6] P. J. Turchi, S. D. Frese, and M. H. Frese, IEEE Trans. Plasma Sci. **45**, 2800 (2017).

[7] S. F. Garanin, IEEE Trans. Plasma Sci. **26**, 1230 (1998).

[8] T. Intrator, S. Y. Zhang, J. H. Degnan, I. Furno, C. Grabowski, S. C. Hsu, E. L. Ruden, P. G. Sanchez, J. M. Taccetti, M. Tuszewski, W. J. Waganaar, and G. A. Wurden, Phys. Plasmas **11**, 2580 (2004).

[9] J. H. Degnan, D. J. Amdahl, M. Domonkos, F. M. Lehr, C. Grabowski, P. R. Robinson, E. L. Ruden, W. M. White, G. A. Wurden, T. P. Intrator, J. Sears, T. Weber, W. J. Waganaar, M. H. Frese, S. D. Frese, J. F. Camacho, S. K. Coffey, V. Makhin, N. F. Roderick, D. G. Gale, M. Kostora, A. Lerma, J. L. McCullough, W. Sommars, G. F. Kiuttu, B. Bauer, S. R. Fuelling, R. E. Siemon, A. G. Lynn, and P. J. Turchi, Nucl. Fusion **53**, 093003 (2013).

[10] M. Laberge, J. Fusion Energy **38**, 199 (2019).

[11] S. A. Slutz, M. C. Herrmann, R. A. Vesey, A. B. Sefkow, D. B. Sinars, D. C. Rovang, K. J. Peterson, and M. E. Cuneo, Phys. Plasmas **17**, 056303 (2010).

[12] M. R. Gomez, S. A. Slutz, A. B. Sefkow, D. B. Sinars, K. D. Hahn, S. B. Hansen, E. C. Harding, P. F. Knapp, P. F. Schmit, C. A. Jennings, T. J. Awe, M. Geissel, D. C. Rovang, G. A. Chandler, G. W. Cooper, M. E. Cuneo, A. J. Harvey-Thompson, M. C. Herrmann, M. H. Hess, O. Johns, D. C. Lamppa, M. R. Martin, R. D. McBride, K. J. Peterson, J. L. Porter, G. K. Robertson, G. A. Rochau, C. L. Ruiz, M. E. Savage, I. C. Smith, W. A. Stygar, and R. A. Vesey, Phys. Rev. Lett. **113**, 155003 (2014).

[13] P. F. Schmit, P. F. Knapp, S. B. Hansen, M. R. Gomez, K. D. Hahn, D. B. Sinars, K. J. Peterson, S. A. Slutz, A. B. Sefkow, T. J. Awe, E. Harding, C. A. Jennings, G. A. Chandler, G. W. Cooper, M. E. Cuneo, M. Geissel, A. J. Harvey-Thompson, M. C. Herrmann, M. H. Hess, O. Johns, D. C. Lamppa, M. R. Martin, R. D. McBride, J. L. Porter, G. K. Robertson, G. A. Rochau, D. C. Rovang, C. L. Ruiz, M. E. Savage, I. C. Smith, W. A. Stygar, and R. A. Vesey, Phys. Rev. Lett. **113**, 155004 (2014).

[14] M. M. Basko, A. J. Kemp, and J. Meyer-ter-Vehn, Nucl. Fusion **40**, 59 (2000).

[15] Y. C. F. Thio, E. Panarella, R. C. Kirkpatrick, C. E. Knapp, F. Wysocki, P. Parks, and G. Schmidt, in *Current Trends in International Fusion Research–Proceedings of the Second International Symposium*, edited by E. Panarella (NRC Canada, Ottawa, 1999) p. 113.

[16] Y. C. F. Thio, C. E. Knapp, R. C. Kirkpatrick, R. E. Siemon, and P. J. Turchi, J. Fusion Energy **20**, 1 (2001).

[17] P. B. Parks, Phys. Plasmas **15**, 062506 (2008).

[18] J. F. Santarius, Phys. Plasmas **19**, 072705 (2012).

[19] S. C. Hsu, T. Awe, S. Brockington, A. Case, J. Cassibry, G. Kagan, S. Messer, M. Stanic, X. Tang, D. Welch, and F. D. Witherspoon, IEEE Trans. Plasma Sci. **40**, 1287 (2012).

[20] C. E. Knapp and R. C. Kirkpatrick, Phys. Plasmas **21**, 070701 (2014).

[21] S. J. Langendorf and S. C. Hsu, Phys. Plasmas **24**, 032704 (2017).

[22] Y. C. F. Thio, S. C. Hsu, F. D. Witherspoon, E. Cruz, A. Case, S. Langendorf, K. Yates, J. Dunn, J. Cassibry, R. Samulyak, P. Stoltz, S. J. Brockington, A. Williams, M. Luna, R. Becker, and A. Cook, Fus. Sci. Tech. **75**, 581 (2019).

[23]S. C. Hsu and Y. C. F. Thio, J. Fusion Energy **37**, 103 (2018).
[24]S. C. Hsu and S. J. Langendorf, J. Fusion Energy **38**, 182 (2019).
[25]J. T. Cassibry, R. J. Cortez, S. C. Hsu, and F. D. Witherspoon, Phys. Plasmas **16**, 112707 (2009).
[26]R. Samulyak, P. Parks, and L. Wu, Phys. Plasmas **17**, 092702 (2010).
[27]T. J. Awe, C. S. Adams, J. S. Davis, D. S. Hanna, S. C. Hsu, and J. T. Cassibry, Phys. Plasmas **18**, 072705 (2011).
[28]J. T. Cassibry, M. Stanic, S. C. Hsu, F. D. Witherspoon, and S. I. Abarzhi, Phys. Plasmas **19**, 052702 (2012).
[29]J. S. Davis, S. C. Hsu, I. E. Golovkin, J. J. MacFarlane, and J. T. Cassibry, Phys. Plasmas **19**, 102701 (2012).
[30]J. T. Cassibry, M. Stanic, and S. C. Hsu, Phys. Plasmas **20**, 032706 (2013).
[31]H. Kim, L. Zhang, R. Samulyak, and P. Parks, Phys. Plasmas **20**, 022704 (2013).
[32]S. C. Hsu, A. L. Moser, E. C. Merritt, C. S. Adams, J. P. Dunn, S. Brockington, A. Case, M. Gilmore, A. G. Lynn, S. J. Messer, and F. D. Witherspoon, J. Plasma Physics **81** (2015).
[33]F. Witherspoon, S. Brockington, A. Case, S. J. Messer, L. Wu, R. Elton, S. C. Hsu, J. Cassibry, M. Gilmore, and the PLX Team, Bull. Amer. Phys. Soc. **56**, 311 (2011).
[34]S. Brockington, A. Case, S. Messer, L. Wu, and F. D. Witherspoon, Bull. Amer. Phys. Soc. **57**, 134 (2012).
[35]A. Case, S. Messer, S. Brockington, L. Wu, F. D. Witherspoon, and R. Elton, Phys. Plasmas **20**, 012704 (2013).
[36]S. Messer, A. Case, L. Wu, S. Brockington, and F. D. Witherspoon, Phys. Plasmas **20**, 032306 (2013).
[37]S. C. Hsu, E. C. Merritt, A. L. Moser, T. J. Awe, S. J. E. Brockington, J. S. Davis, C. S. Adams, A. Case, J. T. Cassibry, J. P. Dunn, M. Gilmore, A. G. Lynn, S. J. Messer, and F. D. Witherspoon, Phys. Plasmas **19**, 123514 (2012).
[38]E. C. Merritt, A. L. Moser, S. C. Hsu, J. Loverich, and M. Gilmore, Phys. Rev. Lett. **111**, 085003 (2013).
[39]E. C. Merritt, A. L. Moser, S. C. Hsu, C. S. Adams, J. P. Dunn, A. Miguel Holgado, and M. A. Gilmore, Phys. Plasmas **21**, 055703 (2014).
[40]A. L. Moser and S. C. Hsu, Phys. Plasmas **22**, 055707 (2015).
[41]S. C. Hsu, S. J. Langendorf, K. C. Yates, J. P. Dunn, S. Brockington, A. Case, E. Cruz, F. D. Witherspoon, M. A. Gilmore, J. T. Cassibry, R. Samulyak, P. Stoltz, K. Schillo, W. Shih, K. Beckwith, and Y. C. F. Thio, IEEE Trans. Plasma Sci. **46**, 1951 (2018).
[42]C. L. Nehl, R. J. Umstattd, W. R. Regan, S. C. Hsu, and P. M. McGrath, J. Fusion Energy **38**, 506 (2019).
[43]S. J. Langendorf, K. C. Yates, S. C. Hsu, C. Thoma, and M. Gilmore, Phys. Rev. Lett. **121**, 185001 (2018).
[44]S. J. Langendorf, K. C. Yates, S. C. Hsu, C. Thoma, and M. Gilmore, Phys. Plasmas **26**, 082110 (2019).
[45]K. Schillo, J. Cassibry, M. Rodriguez, and S. Thompson, J. Nucl. Eng. Rad. Sci. **5**, 042201 (2019).
[46]W. Shih, R. Samulyak, S. C. Hsu, S. J. Langendorf, K. C. Yates, and Y. F. Thio, Phys. Plasmas **26**, 032704 (2019).
[47]E. C. Merritt, A. G. Lynn, M. A. Gilmore, and S. C. Hsu, Rev. Sci. Instrum. **83**, 033506 (2012).
[48]E. C. Merritt, A. G. Lynn, M. A. Gilmore, C. Thoma, J. Loverich, and S. C. Hsu, Rev. Sci. Instrum. **83**, 10D523 (2012).
[49]J. J. MacFarlane, I. E. Golovkin, P. R. Woodruff, D. R. Welch, B. V. Oliver, T. A. Mehlhorn, and R. B. Campbell, in *Inertial Fusion Sciences and Applications 2003*, edited by B. A. Hammel, D. D. Meyerhofer, and J. Meyer-ter-Vehn (American Nuclear Society, 2004) p. 457.
[50]R. P. Young, C. C. Kuranz, D. Froula, J. S. Ross, and S. Klein, Phys. Plasmas **26**, 012101 (2019).
[51]J. D. Huba, *NRL Plasma Formulary*, NRL/PU/6790–18-640 (2018).